Supplement of Atmos. Meas. Tech., 19, 2379–2405, 2026
https://doi.org/10.5194/amt-19-2379-2026-supplement


Atmospheric Measurement Techniques
Open Access
EGU

*Supplement of*

# Modification and validation of a commercial dynamic chamber for reactive nitrogen and greenhouse gas flux measurements

**Moxy Shah et al.**

*Correspondence to:* Trevor C. VandenBoer (tvandenb@yorku.ca)

## S1. Chamber customized components and LabVIEW software

To meet the performance requirements for measuring $N_r$ gases, chamber modifications were implemented to create inert surfaces that transmit them effectively to downstream gas analyzers. In addition, a reference chamber with an inert surface at the bottom (Figure S1) was required to benchmark the performance of a modified chamber (Figure S2) where fittings and surfaces identified to be reactive or to facilitate stronger surface interactions were replaced with more inert components.

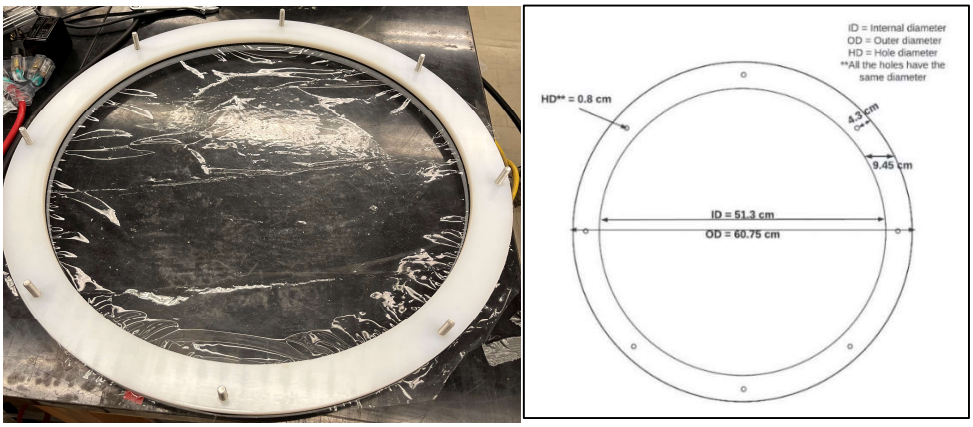


**Figure S1.** (left) Image of the custom-made base rings made from 1.2 cm thick PTFE with a PFA film pinned between them; all the holes have identical diameters, are located equidistant from the edges of the plate and can fit M8 bolts secured with corresponding nuts (McMasterr-Carr®, PN: 90591A161 and 91263A918). (right) Technical scale drawing of a custom-made ring for the chambers with the inner diameter, outer diameter, ring width, and diameter of holes and their distance from the outer edges denoted.

A custom LabVIEW program was created to automate control of the solenoid valves and mass flow controller in the measurement set up using the microcontroller. The front panel of the LabVIEW program (Figure S3a) allows for the timings of the solenoid valve changes to be manually set, along with the log intervals. The VI controls valve states (i.e., for V1, V2, and V3) and synchronization of the valve switching with respect to each chamber opening and closing cycle as described in the previous section. The VI also generates its own text file containing valve open/close state and a timestamp to be used for data processing. A custom R script (R Studio v3.0.1) was developed to process the data file generated by eoslink-AC, data from all reactive gas analyzers, and the VI. A graphical representation of the valve states in real time is included on the front window to allow for the user to assess the measurement state. In the back window (Figure

S3b), the valve timings are controlled within a state machine to allow for continuous valve switching at the time interval selected on the front window. The MFC flow rate is controlled by sending the required voltage to the MFC. The data logging of the valve switching timings and MFC flowrates are handled as well within a state machine to ensure continuous logging to a csv file. The LabVIEW VI is available on the GitHub repository (https://github.com/fjs-vdblab/fluxchamber.git).

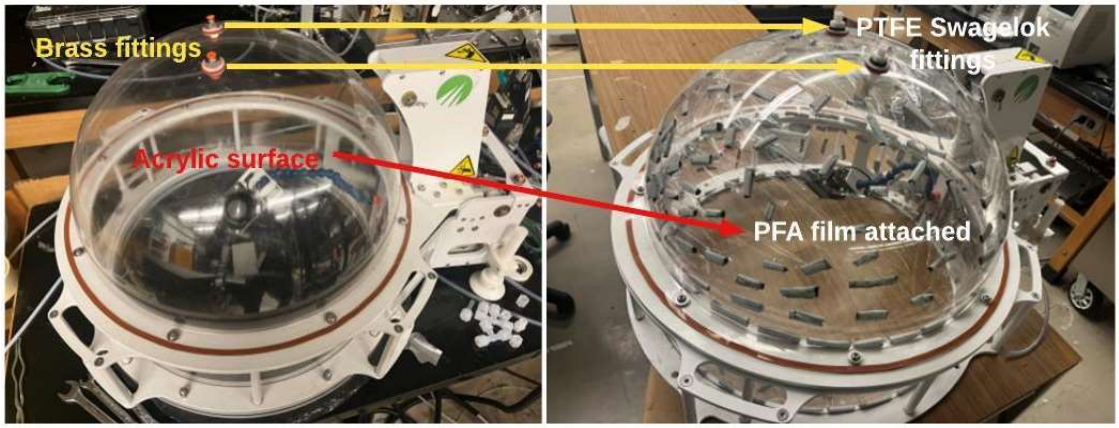


**Figure S2.** (left) The chamber is in its original configuration from the manufacturer with brass push-connect inlet and outlet fittings and an acrylic dome. (right) The modified chamber with 1/4" PTFE Swagelok bulkhead fittings and an attached film of PFA on the interior of the acrylic dome and all chamber sidewalls using adhesive tape.

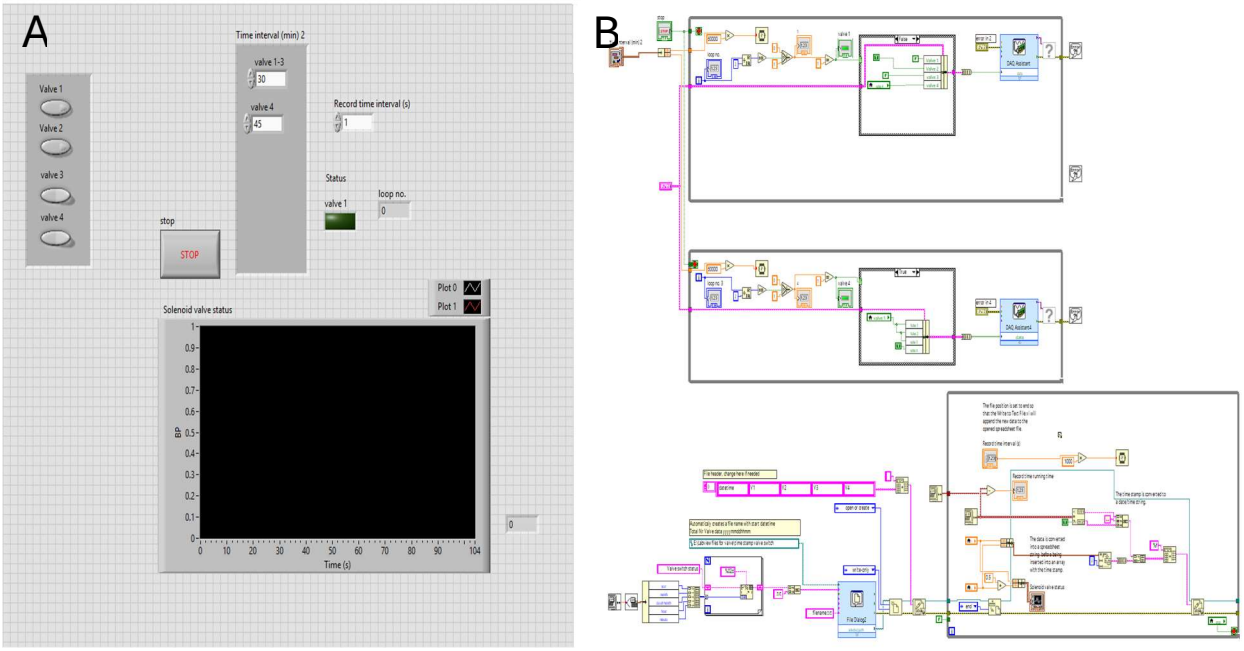


**Figure S3.** Screenshot of our custom LabVIEW VI for controlling the reference and measurement chambers (A) flows, valve states, timing for lid closures, and rate of datalogging through a graphical user interface front window, and (B) the back window virtual machines controlling the objects, voltages, and data flows.

## S2. Gas analyzer quality control procedures

The $NO_x$ analyzer is calibrated with multipoint NO and $NO_2$ mixing ratios to generate calibration curves on at least an annual basis, with span checks and blanks performed regularly prior to the collection of experimental data. For field use, a full calibration is performed prior to relocation of the system to the deployment site, a span check on site, and again at the end of the deployment period to account for any instrumental drift. Zero air from a gas-calibration instrument (Gascal 1100TS, American Ecotech, Warren, RI) is introduced to the analyzer through the sampling inlet to set the zero point. If the NO, $NO_2$ and $NO_x$ readings are within ±0.5 ppbv of one another, the zero offset is calculated and applied. Then, an NO span check is performed using a known mixing ratio from a certified cylinder (e.g. Praxair, NI NO5MC-A3, 4.88 (±5 %) ppmv, Toronto, ON) to ensure the NO and $NO_x$ readings are within ±1 ppbv of the true value. Next, a multi-point precision check of NO is performed at 40 ppbv, 60 ppbv, and 80 ppbv for 30 min, ensuring a stable signal has been achieved. The calibration is considered successful when the analyzer's response to changes in NO mixing ratio is linear, with a slope of 1.00 ± 0.02 and $R^2$>0.98. For multi-point precision checks of $NO_2$, 40 ppbv, 60 ppbv, and 80 ppbv were produced using gas-phase titration

of excess NO with $O_3$, again using the GasCal. The criteria for a successful calibration are the same as described for NO. Conversion efficiency (CE) of $NO_2$ to NO in the analyzer is the final parameter to be quantified, and a CE > 96% indicates that the molybdenum catalyst in the analyzer is operating reliably.

Nitrous acid (HONO) was generated using our in-house calibration source based on the reaction between gas-phase hydrochloric acid (HCl) and a $NaNO_2$ crystalline film on the surface of PFA tubing (RS1) at 50% RH to generate gas-phase HONO and to confirm its unity conversion (Lao et al., 2020).

$$NaNO_{2(s)} + HCl_{(g)} \rightarrow HONO_{(g)} + NaCl_{(s)} \quad \text{(RS1)}$$

In the HONO calibration source, a flow of dry carrier gas (Air Ultra Zero, 99.999%, AI 0.0UZ-K, Praxair) at 50 $cm^3$ $min^{-1}$ passes through a permeation device (PD) containing HCl solution, heated to 30-40 °C. Another 50 $cm^3$ $min^{-1}$ passes through a glass impinger containing deionized water to become saturated with water vapour, so the flow obtains an RH of 50% when combined with that of the HCl. This HCl-water vapour mixture enters a $NaNO_2$-coated PFA reaction device, and HONO is released by acid displacement. A delivered mixing ratio of 10-100 ppb was found to be effectively converted, in line with the performance we have previously described in detail.

Calibration for the $O_3$ analyzer involves a multipoint check, after one hour of warmup time to ensure lamp stability, using 100, 200, 300, and 400 ppbv mixing ratios. The procedure is considered successful if the slope falls between 0.98 and 1.02, the y-intercept between -2 and 2 ppb, and an overall $R^2 > 0.99$.

The calibration and precision check procedure for the Picarro G2509 involved measuring multiple known concentrations of GHGs from a calibration cylinder. The calibration cylinder contained a custom blend of GHGs (4.30 ppm (±5%) $N_2O$, 24.8 ppm (±5%) $CH_4$, 3587 ppm (±2%) $CO_2$), which was a certified standard grade in an air matrix (Linde Canada Plc; PN: AI CD.4MN1C-A3; CGA-590). Pure nitrogen and three calibration points at none, 4.5, and 10-times dilution of the original GHG mixing ratios in the cylinder were delivered to the Picarro analyzer until stable responses were achieved, in triplicate. The custom-built permeation oven for HONO was also used to generate known mixing ratios of $NH_3$ by quantification of bubbler-scrubbed $NH_3$ using ion chromatography (Salehpoor and VandenBoer, 2023). A dry 90 $cm^3$ $min^{-1}$ zero air flow was passed over a PD containing $NH_4OH$ (30% v/v in 1/8" OD tubing with a 9 cm length). Calibration was

performed for mixing ratios of 30 ppbv to 110 ppbv. The dilution of gases was achieved by combining the flow from a liquid $N_2$ dewar (Linde Canada Plc, PN: NI LC250-230). The observed versus returned slopes of 0.99 for $N_2O$, 0.99 for $CH_4$, 0.98 for $CO_2$, and 1.37 for $NH_3$ when compared to the known concentrations delivered, thereby demonstrating suitable and stable calibration of the instrument, as these slopes are within the cylinder or IC mixing ratio uncertainties.

**S3. Gas handling for chamber filling and emptying challenge experiments**

Dilution and analyte gas flow rates were controlled using MFCs (10 L $min^{-1}$, PN: 1179C01314CR1BV, MKS instruments Inc, Andover, MA, US). Mixing ratios of $CO_2$, $CH_4$ and $N_2O$ were controlled by dilution of a calibration gas cylinder containing a custom blend of the three gases (4000 ppm $CO_2$, 20 ppm $CH_4$, 3.3 ppm $N_2O$ in zero air from Linde Canada). Known concentrations of NO and $NO_2$ were added from their respective calibration gas cylinders (5.9 (±5 %) ppmv of NO in air, PN: NI NO5MC-A3; 4.5 (±5 %) ppmv $NO_2$ in air, PN: NI NX5MC-AQ; Linde Canada plc, Toronto, ON). Production of known mixing ratios of $O_3$ to the chamber was achieved by combining output from the built-in ozone generator and photometer of the GasCal into dilution gas at 2 L $min^{-1}$. The 100 $cm^3$ $min^{-1}$ flow of HONO exiting the calibration source was diluted using ZA and mixing ratios spanning 10-100 ppbv were obtained, with 2 L $min^{-1}$ directed to the experimental setup. For NH3, the permeation device output was also diluted with 2 L $min^{-1}$ of zero air to generate a mixing ratio on the order of 30 ppbv.

The time response of gases for the fill and empty process was calculated from the time required to fill the chamber and empty the chamber (Figure S4). It can be described by a single exponential function for non-reactive gases such as $N_2O$, $CH_4$, $CO_2$, and NO and thus the time response, $\tau$, for the exchange of sample gases volume (Section 2.1; E1-4). The double exponential function was used for surface-sensitive and reactive gases, such as $NO_2$, HONO, and $NH_3$, to yield two time constants, $\tau_1$ and $\tau_2$, the time response towards the exchange of the sample air volume and wall interactions (S1), respectively (Ellis et al., 2010).

$$f(t) = y_0 + A_1 \times \exp\left(\frac{-(t-t_0)}{\tau_1}\right) + A_2 \times \exp\left(\frac{-(t-t_0)}{\tau_2}\right) \quad \text{S1}$$

Where $t_0$ is the start time and $y_0$ is the offset that represents the measurement baseline level, $A_1$ and $A_2$ are proportionality coefficients from the contribution of the physical processes of sample volume exchange in the chamber, and reaction and wall interactions, respectively. The relative role of wall interactions or reactions, D, to the overall transfer of gases through a handling system is determined by the contribution of the $A_2$ term to the sum of both A terms (S2).

$$D = \left(\frac{A_2}{A_1 + A_2}\right) \times 100\% \qquad \text{S2}$$

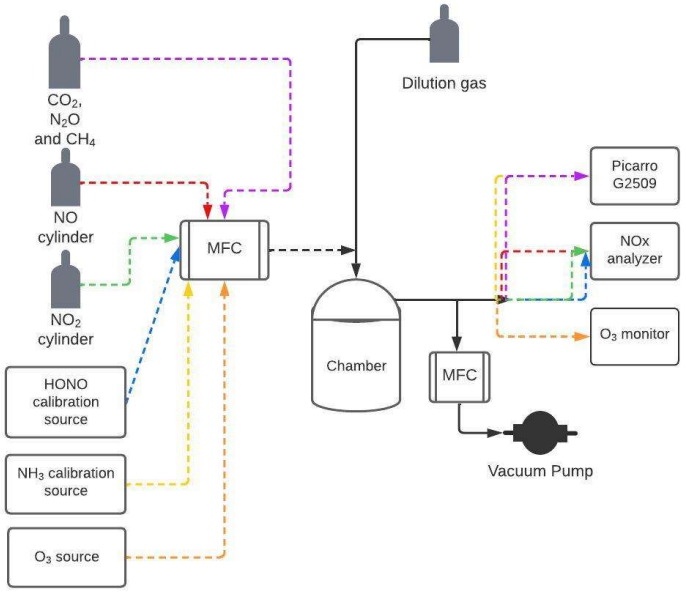


**Figure S4.** Experimental setup to perform fill/empty experiments in the chambers with greenhouse gases: $CH_4$, $CO_2$ and $N_2O$ (purple); $N_r$ gases NO (red), $NO_2$ (green), HONO (blue), $NH_3$ (yellow), and $O_3$ (orange); and dilution gas (black). Dashed arrows show the flow of gases from their respective sources for filling experiments to their respective gas analyzers. Emptying experiments use dilution gas alone once a steady state of the challenge gas has been obtained in the chamber.

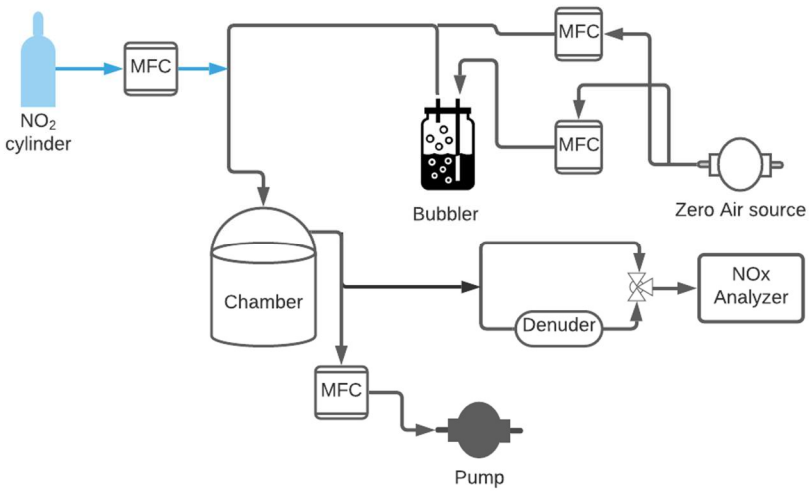


**Figure S5.** Experimental setup for $NO_2$ surface loss characterization, where arrows indicate direction of gas flows. Characterization of losses or transformation to HONO was made by a modified $NO_x$ analyzer with experimental flow balance by an added MFC and pump.

## S4. Multiplexer modification tests on gas transfer of $N_r$ and GHGs

A 2 L $min^{-1}$ flow of dry zero air containing 0.058 ppm of $N_2O$, 0.57 ppm of $CH_4$, and 81.5 ppm of $CO_2$, was passed through a multiplexer equipped with either PTFE or stainless-steel (SS) valves and fittings for 30 min to access relative losses. A separate experiment was performed with 2 L $min^{-1}$ zero air containing a known concentration of $NH_3$ (0.41 ppm), which was generated based on the method described in Crilley et al. (2023) from a permeation tube containing $NH_4OH$. Similarly, the transfer efficiency of $NO_2$ was determined using a calibration cylinder (Linde Canada; PN: NI NX5MC-AQ; 5.9 (±5%) ppm) which was combined with a 2 L $min^{-1}$ dilution flow of dry ZA to achieve a mixing ratio of 54 ppb. All challenge gases were passed through the multiplexer equipped with either PTFE or SS valves and PFA or SS fittings, respectively, to assess relative losses. All delivered and exiting flows were confirmed to be equal during these tests, ensuring no leaks led to a measured loss. The loss percentage in SS fittings and gas handling valves was measurable but generally remained below 20%, except for $NH_3$, which exhibited a 38% reduction. With the modifications, minimal surface loss of GHGs and $NO_2$ (<1%) was observed when using the PFA fittings and PTFE valves, whereas $NH_3$ exhibited a reduced 11% loss (Figure S6).

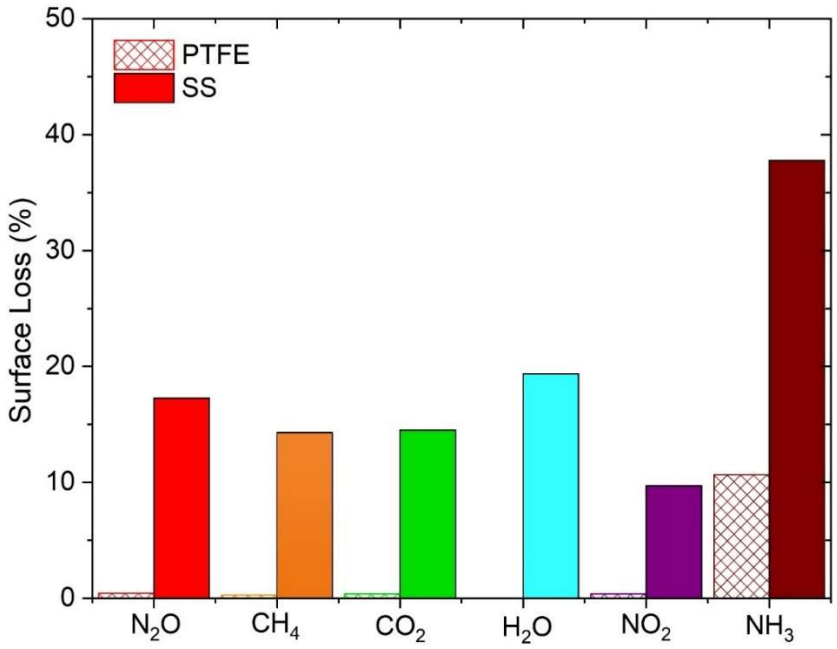


**Figure S6**. Loss percentage of GHGs ($N_2O$, $CH_4$, $CO_2$,) and $N_r$ ($NO_2$, $NH_3$) gases on stainless steel fittings than that of a PTFE valve and unions.

The surface porosity of SS can influence its adsorption capacity for $CH_4$ through van der Waals interaction potentials (Sapag et al., 2010). Previous studies have shown that passivation of the SS surface via NO treatment can remove surface iron and promote the formation of chromium-enriched oxide films, which in turn govern the surface chemical reactivity toward NO (Ma et al., 2020). Furthermore, thin layers of iron oxides formed on SS surfaces can affect the interaction with $N_2O$ and alter its decomposition pathways. Consequently, the combined effects of SS surface porosity on $CH_4$ van der Waals interactions, chromium-oxide passive films influencing NO reactivity, and iron-oxide layers acting as active adsorption sites for $N_2O$ may contribute to up to a 20 % loss of these gases on SS surfaces. It is likely that the surface losses observed here for very clean SS purged extensively with dry zero air prior to these experiments is passivated over time when exposed to ambient air continuously, where the surface adsorption sites are fully occupied and losses no longer occur.

## S5. Chamber modification impacts on gas transfer of $NO_2$ and materials for $O_3$

Gas interactions on chamber surfaces during challenge experiments were reversible for all $N_r$ and GHGs tested, except $NO_2$, which showed reactive losses. These were characterized by calculating

the lost fraction from a small 5 ppb mixing ratio delivered into an unmodified chamber at a high relative humidity of 83%, followed by modifications to reduce this outcome under these challenging simulated environmental conditions (Figure S5). Replacement of the brass push-to-connect fittings delivered the greatest reduction in reactive losses of $NO_2$, with modest gains obtained from covering chamber surfaces with the PFA film (Figure S7). The final lost fraction of $NO_2$ in the modified system reported here is technically at the modified $NO_x$ analyzer detection limit and therefore represents a conservative upper limit estimate.

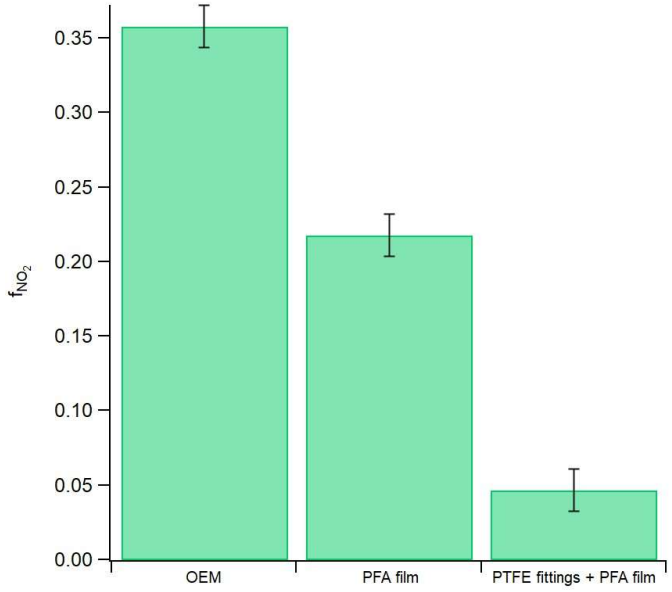


**Figure S7.** Average $NO_2$ loss fraction observed upon addition of 5 ppbv of $NO_2$ at 83% RH to an eosAC-LT® chamber (n = 3 each). These trials were conducted in chambers sequentially: without any modifications (original equipment manufacturer; OEM), following attachment of a PFA film to the inner surface (PFA film), and replacing brass-lined push to connect fittings with ¼" PTFE Swagelok bulkhead (PTFE fittings + PFA film).

Different RH values were produced inside the flux chamber by combining flows of dry zero air (ZA) and one saturated with water vapour by transiting a 500 mL Pyrex impinger filled with deionized water (e.g. equal 1 L $min^{-1}$ flows combine to an RH of 50%). A high-precision, research-grade humidity probe (HMP60, Vaisala Oyj, Finland; ± 3% at 0 - 90% RH, ± 5% at 90 – 100% RH) was connected to the chamber to confirm the set point by measurement in the chamber. The flow from an $NO_2$ calibration cylinder (Linde Canada; PN: NI NX5MC-AQ; 5.9 (±5%) ppm) was adjusted using an MFC and combined with a dilution flow of ZA to achieve mixing ratios of 5, 7 and 10 ppbv. The total flow rate for these experiments was 2.0 L $min^{-1}$ and a vacuum pump (62.3

L $min^{-1}$, PN: UZ-07061-22, Gast Manufacturing Inc., Benton Harbor, MI, USA) with an MFC (10 L $min^{-1}$, PN: 1179C01314CR1BV, MKS instruments Inc, Andover, MA, US) was used to make up the sampling flow beyond the 0.5 L $min^{-1}$ of the $NO_x$ analyzer. The same flow difference stated above was maintained in the chamber, using the built-in vent.

Prior to $O_3$ addition, in the characterization experiments, the chamber was flushed with ZA until the background level of $O_3$ was at the instrument detection limits. Three mixing ratios of $O_3$ of 150, 200 and 250 ppb generated by a GasCal 1100 dilution calibrator with integrated $O_3$ generator and photometer (American Ecotech, Warren, RI) and added to the chamber for 60 mins or until a constant concentration was reached. Two replicate runs of each addition level were performed and delivered mixing ratios were confirmed from bypassing the chambers with just the 15 m gas handling lines.

Ozone is known to undergo heterogeneous surface reactions, particularly on materials like glass, metals, or polymers (Plake et al., 2015). These surfaces often contain reactive sites such as hydroxyl groups or adsorbed water molecules that can catalyze the decomposition of $O_3$ into molecular oxygen ($O_2$) and other byproducts (George et al., 2015). Adsorption of $O_3$ on chamber surfaces is another potential pathway for loss. When $O_3$ molecules interact with surfaces, they may undergo a reaction if the materials are not inert. The use of PFA here was intended to benefit the transfer of $O_3$, yet despite its high chemical inertness, low reactivity, and resistance to the uptake of many chemicals from gas samples, the subsequent $O_3$-driven surface reactions are still substantial (Ebnesajjad, 2017). This is likely because, over time, reactive substances from sampled air accumulated through adsorption on the PFA film and/or its defect sites, thereby reducing its effectiveness. The same issue is well-known for PFA tubing used in standard air quality monitoring and is a common maintenance need for $O_3$ analyzer inlets. Further, physical wear or surface aging might alter the material surface through product formation or exposure of new reaction sites, which makes it less resistant to further reaction with $O_3$, and therefore increases the rate of loss over time. This is the case in our aged PFA film results, which emphasizes the importance of regular replacement of the film as part of the $N_r$ system maintenance and that quality control procedures characterizing the chamber material performance with respect to $O_3$ will provide the highest accuracy of experimental results.

## S6. Agricultural soil samples used for laboratory $N_r$ emission measurements

A systematic method was used to collect soil samples from an agricultural field to avoid sampling bias, assuming there is no topographic reason for differences in soil properties and nutrient content within the specified plot area. The total field area was divided into eight identical plots (A-H) of 10,800 $m^2$ (120 m × 90 m). Soil samples were collected from four random coordinates within each plot, assuming that samples collected within 1 $m^2$ were homogeneous. An approximate 1 L soil core ~15 cm deep was collected with a clean shovel into a pre-labelled clean Ziploc bag. All soil samples were stored below 10 °C and transported to the laboratory within a week.

Four within-plot samples were collected to better approximate soil properties and nutrient content across the entire field. A total of 32 soil samples were collected from the field, where three of the randomly collected within-plot samples were combined generate a plot scale sample, and one sample within each plot was randomly selected to be combined into a pooled sample representative of the field scale. For the purposes of this work, we assessed the emissions of NO, $NO_2$, and HONO from duplicate pooled samples and from Plot D within this sampling experiment (Figure S8).

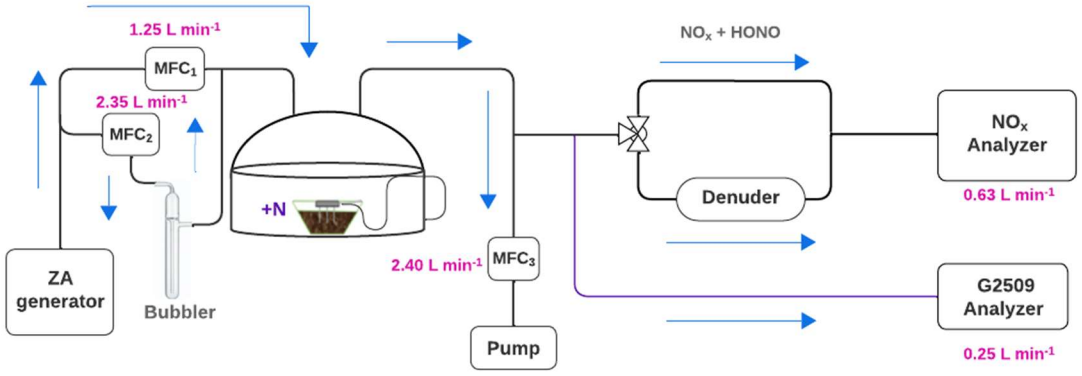


**Figure S8.** Schematic representation of a dynamic chamber system to measure NO, $NO_2$, and HONO fluxes with a modified $NO_x$ analyzer (black lines) and $NH_3$ and $N_2O$ for soil amended with fertilizer using G2509 (purple line). Zero air and humid airflow rates were set using MFC 1 and MFC 2, for a total of 3.6 L $min^{-1}$ going into the chamber. The three-way valve either sends headspace air directly to the $NO_x$ analyzer (measures NO and $NO_2$+HONO), or via the $Na_2CO_3$-coated denuder (measures NO, and $NO_2$). Blue arrows indicate the flows throughout the experimental setup, with flow rates provided in pink text.

Soil $NH_3$ and $N_2O$, along with NO, $NO_2$, and HONO, were measured when the pooled soil sample was amended with four different nitrogen salts (i.e., AN, urea, ABC, AC; Table S1, Figure 4). For

each experiment, 350 g of soil was used, and a corresponding fertilizer solution equivalent to 100 kg N $ha^{-1}$ was added. Additional experimental details are provided in Section 2.5.1 of the main manuscript. The interpretation of the full set of experimental results will be presented in a forthcoming publication on field-scale heterogeneity of $N_r$ emissions and comments on the assumption that individual samples represent these processes across fields with similar physicochemical properties.

**Table S1.** The average and integrated flux for soil treated with 4 different nitrogen salts (urea, ammonium bicarbonate (ABC), ammonium carbonate (AC), and ammonium nitrate (AN)). Average fluxes were calculated over the entire experimental cycle. Integrated fluxes were obtained using the trapezoidal rule. Standard deviations reflect the variability in fluxes measured across the time points for the single sample analyzed per treatment. Replicates of urea (~40 hours) and AN (~5 hours) were analyzed with only the modified $NO_x$ analyzer, thus lacking data for $N_2O$ and $NH_3$ (represented by -).

| Soil sample | Avg Flux (μg N $m^{-2}$ $hr^{-1}$) | | | | | Integrated flux (μg N $m^{-2}$) | | | | |
|---|---|---|---|---|---|---|---|---|---|---|
| | NO | $NO_2$ | HONO | $N_2O$ | $NH_3$ | NO | $NO_2$ | HONO | $N_2O$ | $NH_3$ |
| Urea | 0.1 ± 0.06 | 0.03 ± 0.01 | 0.002 ± 0.004 | 9 ± 3 | 1 ± 0.5 | 230 | 120 | 1 | 32400 | 3700 |
| ABC | 0.03 ± 0.01 | 0.1 ± 0.01 | 0.03 ± 0.02 | 7 ± 6 | 20 ± 7 | 90 | 300 | 90 | 25300 | 85900 |
| AC | 0.03 ± 0.004 | 0.2 ± 0.03 | 0.01 ± 0.01 | 3 ± 2 | 20 ± 3 | 90 | 500 | 1 | 9600 | 63700 |
| *AN | 1 ± 0.1 | 1 ± 0.1 | 1 ± 0.02 | - | - | 50 | 50 | 40 | - | - |

## S7. Analytical solutions to soil reactive gas flux determination with a two-chamber setup

For a single chamber system, S3 can be used to calculate the gas flux to and from an enclosed surface. Each of these terms and their units is provided in Section 2.6 of the main manuscript.

$$V\frac{dC_{\text{cham}}(t)}{dt} = (A \cdot F_{\text{soil}}(t)) + (Q_{\text{in}} \cdot c_{\text{in}}(t)) - (Q_{\text{out}} \cdot c_{\text{out}}(t)) + (V \cdot R(t)) \quad \text{S3}$$

Where V is the volume of the chamber ($m^3$), $A$ is the surface area ($m^2$) enclosed by the chamber and governing the gas flux; $Q_{out}$ is the volumetric flow rate of air exiting the chamber ($m^3\ s^{-1}$; $c_m(t)$ and $c_r(t)$ are target gas concentrations within the measurement and reference chamber (mol $m^{-3}$), respectively; $c_{in}$ and $c_{out}$ represent their corresponding rates of change (mol $m^{-3}\ s^{-1}$); and $F_{net}$ is the resulting net gas flux per unit area (mol $m^{-2}\ s^{-1}$). The terms $R_r$ denote the instantaneous chemical production or loss rate expressed in units of mol $m^{-3}\ s^{-1}$ for consistency.

In our field pilot study, the measurement and reference chambers were installed on clay soil using serrated collars inserted about 10 cm deep into pre-dug circles (30 cm diameter, 20 cm depth) between crop rows of senescing soybeans after removing debris. Collars were left to settle for over 24 hours before the chambers were bolted securely to ensure a gas-tight seal. Flux observations were made for two weeks from 02-16 September 2022, during a period when daytime air temperatures were regularly over 25 °C, and there were no instances of rain. During the second week of observations, a fertilizer addition of 25 kg N $ha^{-1}$ was made by broadcasting urea in the chamber, followed by applying clean water to simulate 2.5 cm (1") of rainfall.

In our sampling setup, there is a negligible concentration of any target gas in the inflow ($c_{\text{in}}(t) \approx 0$) due to the use of ultra-pure zero air or nitrogen, and the air is actively mixed inside the chamber with its fan, such that $c_{\text{chamb}} = c_{\text{out}}$, so the equation simplifies to Equation S4. For non-steady-state conditions, where the concentration inside the chamber is changing over time, the time-varying nature of the sources and sinks needs to be accounted for. The instantaneous equation that describes the behaviour over an interval [$t_1$, $t_2$] is the integral in Equation S5.

$$V\frac{dC_{\text{cham}}(t)}{dt} = (A \cdot F_{\text{soil}}(t)) - (Q_{\text{out}} \cdot c_{\text{cham}}(t)) + (V \cdot R(t)) \quad \text{S4}$$

$$\int_{t_1}^{t_2} V\frac{dC_{\text{cham}}(t)}{dt}\,dt = \int_{t_1}^{t_2}\left[(A \cdot F_{\text{soil}}(t)) - (Q_{\text{out}} \cdot c_{\text{cham}}(t)) + (V \cdot R(t))\right]\,dt \quad \text{S5}$$

Assuming the soil flux, $F_{soil}$ (mol $m^{-2}$ $s^{-1}$), is constant over the time interval [$t_1$, $t_2$] is a reasonable assumption for experimental setups where the environmental conditions and, where relevant, soil-plant activity, do not change substantially over short periods of a few to tens of minutes (Pape et al., 2009). Rearranging the expression for Equation S5, a flux can be calculated using Equation S6.

$$F_{soil} = \frac{V\Delta C_{\text{cham}} + Q_{\text{out}} \int_{t_1}^{t_2} c_{\text{cham}}(t)\, dt - \int_{t_1}^{t_2} R(t)\, dt}{A(t_2 - t_1)} \quad \text{S6}$$

The volumetric mixing ratio (Equation S7) is often the unit of measurement for many gas analyzers and defined as the number of moles of the gas divided by the number of moles of dry air. The mixing ratio $X$ is dimensionless and provides a way to express gas concentrations independently of changes in temperature or pressure.

$$X = \frac{n_{\text{gas}}}{n_{\text{air}}} \quad \text{S7}$$

We can then write the molar concentration, c (mol $m^{-3}$), in the form of volumetric mixing ratio using Equation S8:

$$c_{\text{chamber}} = X_{\text{out}} \times \rho_d \quad \text{S8}$$

Here, $\rho_d$ (mol $m^{-3}$) is the molar density of the air. The total pressure $P$ is equal to atmospheric pressure, such that by using the ideal gas law, we can define the density of air using Equation S9:

$$\rho_d = \frac{P}{R \cdot T} \quad \text{S9}$$

Where $P$ (Pa) is the pressure, $R$ (J $mol^{-1}$ $K^{-1}$) is the universal gas constant, and $T$ (K) is the absolute temperature. In Equation S9 it is assumed that atmospheric air behaves as an ideal gas, which is a reasonable approximation under typical environmental conditions, even at the Earth's surface. The resulting molar concentrations can then be calculated and used in the flux determinations as presented in Equations 6 and 7 in the main manuscript.

### S7.1 Dynamics and physical corrections from reference and measurement chambers

In environmental and experimental settings where gas flux is measured, it is important to capture the rate at which gas concentrations change over time. This rate reflects the net outcome from both gas emission and deposition occurring simultaneously, influenced by the surface under study,

temperature, pressure, flow, and surface interactions (Equation S10). The RC (r), which operates under identical conditions to the MC (m) but excludes the surface under study by isolating it beneath the PFA film, takes into account the environmental and surface effects, such that its observed flux rate is described by Equation S11. To isolate the effects of the surface under study from reactions taking place in the atmospheric sample and on the chamber surfaces, the rate of change in the RC is subtracted from that in the MC, yielding the net flux through Equation S12.

$$F_m = surface\ under\ study + environmental\ and\ chamber\ effects \quad \text{S10}$$

$$F_r = environmental\ and\ chamber\ effects \quad \text{S11}$$

$$F_{net} = F_m - F_r \quad \text{S12}$$

The net rate of change can now be used to calculate the molar flux by substituting it into Equation S6 to arrive at Equation S13, which is the core of Equation 6.

$$F_{\text{net}} = \frac{V}{A}\left(\frac{\Delta C_m}{\Delta t_m} - \frac{\Delta C_r}{\Delta t_r}\right) + \frac{Q_{\text{out}}}{A}\left(\frac{\int_{t_{1m}}^{t_{2m}} c_m(t)\ dt}{\Delta t_m} - \frac{\int_{t_{1r}}^{t_{2r}} c_r(t)\ dt}{\Delta t_r}\right) - \frac{V}{A}\left(\frac{\int_{t_{1m}}^{t_{2m}} R_m(t)\ dt}{\Delta t_m} - \frac{\int_{t_{1r}}^{t_{2r}} R_r(t)\ dt}{\Delta t_r}\right) \quad \text{S13}$$

The closure period of the two chambers is matched to facilitate an accurate correction of the kinetics and surface interactions. The calculated flux from the surface under study is therefore corrected for background and environmental effects, reducing systematic bias from gas reactivity.

Last, we introduce a flux attenuation factor ($\lambda$; Equation S14) to correct for partial transmission of a targeted reactive gas due to adsorption to chamber walls and gas handling lines during a measurement cycle ($t_1$-$t_2$). This factor needs to be determined empirically through calibration experiments, like those presented in Figure 2, where the loss of the surface-active gas is quantified relative to the transmission of inert gas during both filling and emptying processes.

$$\lambda = \frac{\int_{t_1}^{t_2}\left(\frac{dX}{dt}\right)_{\text{theoretical}} dt}{\int_{t_1}^{t_2}\left(\frac{dX}{dt}\right)_{\text{measured}} dt} \quad \text{S14}$$

We can account for $\lambda$ in Equation S13, to get the molar flux of gas inside the chamber, which accounts for flux loss (Equation S15) by scaling the equation directly to arrive at the full form presented as E6 in the main manuscript.

$$F_{\text{net}} = (\lambda).\left(\frac{V}{A}\left(\frac{\Delta C_m}{\Delta t_m} - \frac{\Delta C_r}{\Delta t_r}\right) + \frac{Q_{\text{out}}}{A}\left(\frac{\int_{t_{1m}}^{t_{2m}} c_m(t)\,dt}{\Delta t_m} - \frac{\int_{t_{1r}}^{t_{2r}} c_r(t)\,dt}{\Delta t_r}\right) - \frac{V}{A}\left(\frac{\int_{t_{1m}}^{t_{2m}} R_m(t)\,dt}{\Delta t_m} - \frac{\int_{t_{1r}}^{t_{2r}} R_r(t)\,dt}{\Delta t_r}\right)\right)$$ S15

## S7.2 Chemical corrections from reference and measurement chambers

For reactive species impacting our $N_r$ suite – mainly NO, $O_3$, and $NO_2$ – flux values can be attenuated or enhanced due to the reaction of NO with $O_3$ (RS2). We show below (Figure S9) that the photolysis of $NO_2$ and HONO is negligible due to the high-energy photon cut-off of acrylic (<400 nm threshold) (RS3). Nevertheless, we include the $NO_2$ photolysis term in the rate expression for completeness, noting that under our field conditions its contribution (Section S7.2.1) is within the noise of the $NO_2$ fluxes. The rate of reactions RS2 and RS3 for $NO_2$, therefore, can be expressed by Equation S16.

$$\mathrm{NO} + \mathrm{O_3} \rightarrow \mathrm{NO_2} + \mathrm{O_2}$$ RS2

$$NO_2 + hv \rightarrow NO + O$$ RS3

$$\frac{d[\mathrm{NO_2}]}{dt} = k_{\mathrm{NO+O_3}}[\mathrm{NO}][\mathrm{O_3}] - J_{\mathrm{NO_2}}[\mathrm{NO_2}]$$ S16

The total change in the concentration due to reaction over a cycle can be expressed by integrating the rate equation over the cycle duration, as the start time ($t_0$) and end time (t) are known, therefore replacing the term $R$ in Equations S15 (and 6 in the main manuscript) with the expression in Equation S17. Under our chamber conditions, the integrated photolysis contribution was smaller than the measurement uncertainty of the $NO_2$ fluxes (Section S7.2.1), and therefore it was not included as an explicit term in Equation S17.

$$\int_{t_0}^{t} R\ d\mathrm{t} = \Delta[\mathrm{NO}] = \Delta[\mathrm{O_3}] = -\Delta[\mathrm{NO_2}] = -\int_{t_0}^{t} k\,[\mathrm{NO(t)}][\mathrm{O_3(t)}]\,d\mathrm{t}$$ S17

Where the R is the loss rate$R \leq 0$ ($O_3$ (R<0) and the simultaneous produc$R \geq 0$ for $NO_2$ (R≥0). For the kinetic determination, number density of the gases (molec $cm^{-3}$) is used to track the chemical transformations over time, but instrumentation typically measures mixing ratios. If temperature and pressure are measured alongside target gases in the dynamic chambers, then using Equations S8 and S9, the reaction-corrected flux based on measured mixing ratios can be calculated using Equation S18.

$$F_{\text{net}} = \lambda \cdot \frac{P_{\text{air}}}{R \cdot T} \cdot \left( \frac{V}{A}\left(\frac{\Delta X_m}{\Delta t_m} - \frac{\Delta X_r}{\Delta t_r}\right) + \frac{Q_{\text{out}}}{A}\left(\frac{\int_{t_{1m}}^{t_{2m}} X_m(t)\,dt}{\Delta t_m} - \frac{\int_{t_{1r}}^{t_{2r}} X_r(t)\,dt}{\Delta t_r}\right) - \frac{V}{A}\left(\frac{P_{\text{air}}}{R \cdot T}\right)\left(\frac{\int_{t_{1m}}^{t_{2m}} k \cdot X_{\text{NO}m}(t) \cdot X_{\text{O3}m}(t)\,dt}{\Delta t_m} - \frac{\int_{t_{1r}}^{t_{2r}} k \cdot X_{\text{NO}_r}(t) \cdot X_{\text{O3}_r}(t)\,dt}{\Delta t_r}\right)\right) \quad \text{S18}$$

Where, again, $P_{air}$ (Pa) the atmospheric pressure inside the measurement and reference chambers, R (J $mol^{-1}$ $K^{-1}$) is the gas constant, and $T$ (K) is the temperature inside the RC and MC. For non-reactive gases like $CO_2$, $CH_4$, and $N_2O$, there is no reaction term, and the flux can be described simply using Equation S19 as below, which is presented as E7 in the main manuscript.

$$F_{\text{net}} = \lambda \cdot \frac{P_{\text{air}}}{R \cdot T} \cdot \left( \frac{V}{A}\left(\frac{\Delta X_m}{\Delta t_m} - \frac{\Delta X_r}{\Delta t_r}\right) + \frac{Q_{\text{out}}}{A}\left(\frac{\int_{t_{1m}}^{t_{2m}} X_m(t)\,dt}{\Delta t_m} - \frac{\int_{t_{1r}}^{t_{2r}} X_r(t)\,dt}{\Delta t_r}\right)\right) \quad \text{S19}$$

### S7.2.1 Losses of $NO_2$ or HONO due to photolysis within transparent chambers

The fraction of $NO_2$ or HONO lost due to photolysis depends on the photons transmitted through the chamber material (Figure S9). The photolysis rate is estimated here under a worst-case scenario with respect to our field observations, using actinic flux data collected for Lambton County, Ontario, Canada, at 12:00 PM local time on September 10, 2022, under clear sky conditions. The effective photolysis rate constant within the chamber was calculated to be 2.62 x $10^{-4}$ $s^{-1}$, using Equation S20.

$$J = \int [\sigma(\lambda) \cdot \Phi(\lambda) \cdot F(\lambda) \cdot T(\lambda)]\, d\lambda \quad \text{S20}$$

Where $\sigma(\lambda)$ is the absorption cross-section of $NO_2$ ($cm^2$ molecule $^{-1}$), $\Phi(\lambda)$ is the quantum yield (dimensionless; 0-1), $F(\lambda)$ is the actinic flux (photons $cm^{-2}$ $s^{-1}$ $nm^{-1}$), and $T(\lambda)$ is the transmission of the acrylic chamber material (dimensionless) at wavelength $\lambda$ (dimensionless; 0-1).

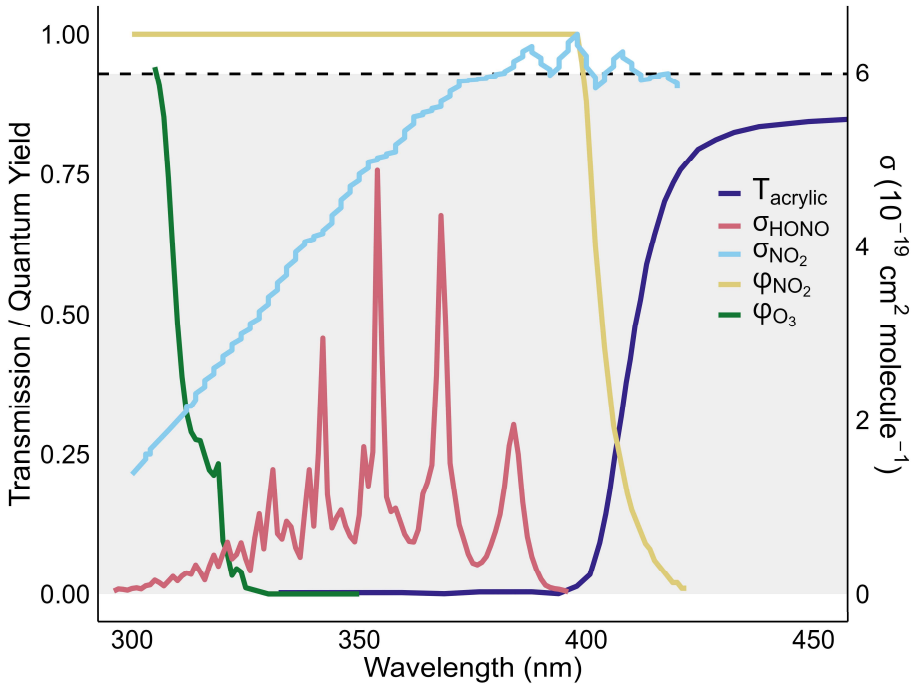


**Figure S9.** Transmission of light through the chamber and quantum yields for photolysis of $O_3$ and $NO_2$, along with the absorption cross section of $NO_2$ and HONO, as a function of wavelength. The shaded region denotes the manufacturer-specified minimum transmission ($\geq$ 93%) for the PFA film. Note the negligible overlap for photodissociation. The acrylic effectively blocks wavelengths below approximately 400 nm, meaning the photolysis rate of $NO_2$ is the only one impacted by a chamber constructed from this material.

Using this attenuated loss rate in a kinetic model, we find that at most 14% of the initial $NO_2$ concentration is lost due to photolysis within the chamber in the first 10 minutes, and 37% within 30 minutes (Figure S10, blue trace). This rate of photolysis significantly reduces the $NO_2$ mixing ratio within the chamber environment. The wavelength cut-off of polyacrylate limits the penetration of shorter wavelengths, which are more effective in driving $NO_2$ photolysis, so the overall rate is slowed inside the chamber compared to ambient conditions (Figure S10, red trace). Despite this, within the initial 30-minute timeframe (Figure S10, vertical dashed line), the change in the fraction of $NO_2$ lost is relatively small due to the dynamic nature of the chamber headspace (i.e. due to continuous sampling and dilution flows), allowing for a reasonable linear approximation of the curve. The photolytic loss of HONO is much more impacted by the cutoff wavelength of the polyacrylate chamber lid, to the point where it is not substantially lost due to photolysis. As shown in Figure S9, the HONO absorption cross-section lies almost entirely below the ~400 nm transmission cutoff of the chamber lid. This spectral mismatch means that HONO photolysis is effectively suppressed inside the chamber, unlike $NO_2$, which still absorbs within the

147 transmitted range. Consequently, chamber-derived HONO fluxes are not biased by photolytic loss,
148 making their interpretation simpler than $NO_2$.

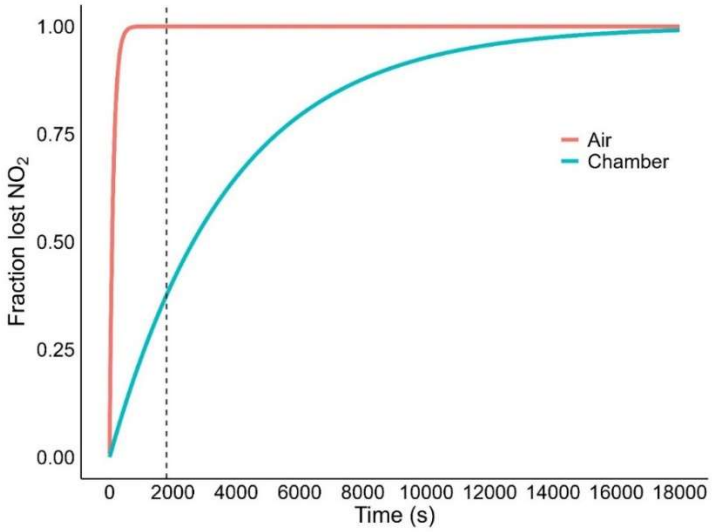


149

150 **Figure S10.** Fraction of $NO_2$ lost due to photolysis over time, both inside the chamber (blue line)
151 and in ambient air (red line). The vertical dashed line indicates the 30-min mark, where an initial
152 linear approximation of the loss rate can be applied.

153 This simplification yields an estimated initial photolysis rate loss of approximately 1% per minute
154 for $NO_2$ over the initial 30-minute measurement cycle and effectively 0% per minute for HONO
155 under chamber conditions due to the cutoff wavelength. This linear approximation is only valid
156 for this kind of short initial period. Beyond 30 minutes, the overall trend exhibits a steeper
157 exponential decay, characteristic of the $NO_2$ photolysis process. This photolysis contribution is
158 included within the reaction term (Equation S16). Its effect (~1% $min^{-1}$ maximum at noon under
159 clear-sky conditions) is smaller than the uncertainties of the $NO_2$ flux measurements, so it is not
160 explicitly propagated into the flux equations in this work.

161

162 **S7.3 Surface interaction correction using the attenuation factor (λ)**

163 Accurate quantification of trace gas fluxes using dynamic chamber systems also requires
164 correction for attenuation caused by gas-wall interactions and the associated sensor response
165 delays. These effects can significantly suppress the measured accumulation rate of reactive species
166 within the closed chamber, particularly for compounds with strong surface affinity, such as $NH_3$,
167 $NO_2$, and HONO, requiring the use of the attenuation factor (λ; Equation S14).

The attenuation factor is derived from our controlled delivery experiments that simulated two sequential measurement scenarios: a filling phase, where gas is introduced and accumulates within the chamber, and an emptying phase, where the chamber is flushed and the gas signal declines (Figure 4). For an ideal gas without wall interactions, the integrated difference between theoretical and observed concentrations within a single chamber should approach zero, and λ would be approximately one. However, as shown in Figure S11, all three gases exhibited surface interactions, with $NH_3$ showing the largest deviation from an inert gas model.

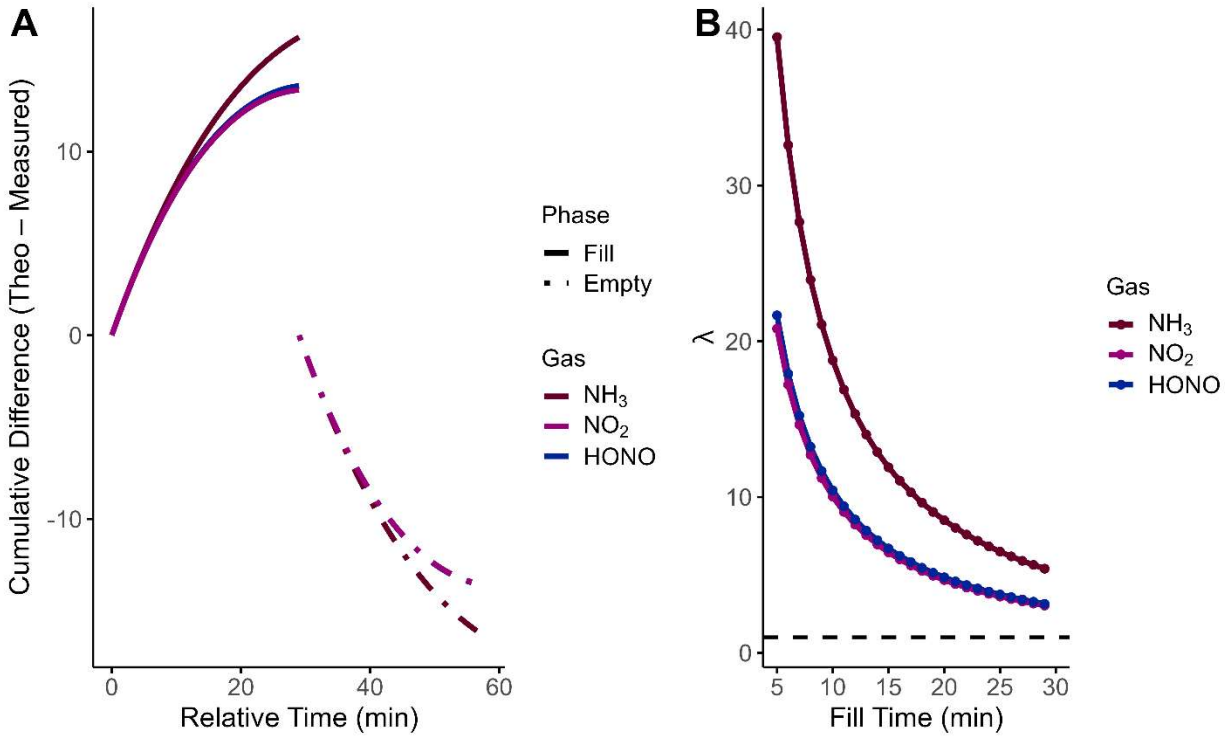


**Figure S11.** (A) Cumulative integration of the difference between inert and measured gas concentrations for $NH_3$, $NO_2$, and HONO over a 30-minute filling and emptying period and (B) resulting λ values for modified chambers, 15 m PFA lines, and gas analyzers as a function of filling time with a dashed line at one corresponding to the transmission of an inert gas. Theoretical concentrations represent expected values from an inert gas without attenuation, while measured values reflect signal loss due to gas–wall interactions. Solid lines correspond to the filling phase; dashed lines represent the emptying phase, together representing a full in situ measurement cycle. These illustrate the time-dependent and nonlinear attenuation that underlies the empirical calculation of λ. Note that due to observations switching to the RC, the emptying phase does not impact the value of λ applied during field use.

When filling, the gas accumulates in the chamber, with a strong initial attenuation that diminishes over time as the surfaces passivate. Conversely, adsorbed gases from surface passivation may partially desorb during emptying, offsetting some of the losses observed during filling. Two respective λ values can be derived and considered separately by integrating the filling and emptying concentration-time series independently.

Where a single-chamber is used to study an experimental system, the filling- and emptying-phase effects offset one another, masking the attenuation as all the surface interacting molecules are eventually transferred to the gas analyzer. In field applications with a dual chamber approach in use, this symmetry is lost because the measurement chamber accumulates a real emission flux during a defined closure period, while the reference chamber does not. Hence, an empirical calculation of λ is needed which compensates for the attenuation in both the accumulation and depletion of the target gas (Table S7). For $NH_3$, the fill-phase difference was 16.23, dividing the expected theoretical accumulation by this measured accumulation yields a $\lambda_{fill}$ of 5.40, while the empty-phase difference was −16.44, with a $\lambda_{empty}$ of 0.36. Unsurprisingly, $NO_2$ and HONO followed a similar trend as we also noted their surface interactions, with $\lambda_{fill}$ values of 3.04 and 3.14 resulting from our characterizations, respectively, and $\lambda_{empty}$ values near 0.40. Uncertainties in λ were quantified from three replicate fill-empty characterizations under identical laboratory conditions, yielding one-sigma deviations of ±0.21 for $NH_3$, ±0.02 for $NO_2$, and ±0.02 for HONO. These values therefore represent attenuation behavior for a pristine or lightly used chamber system.

From a physical and mathematical standpoint, attenuation reduces all concentration-dependent components of the flux (accumulation/depletion, dilution, and reaction) by the same factor. As a result, the attenuation factor λ scales the entire net-flux expression rather than only the accumulation term. Because λ depends on surface condition, extended field use or residue accumulation may alter its value, and periodic re-characterization is recommended to maintain accurate flux estimates.

**Table S7.** The cumulative integrated differences between theoretical and measured values from Figure S11 for both the filling and emptying phases, and the resulting λ values. While the signed fill and empty values appear approximately balanced, their directional impact differs, and the underlying asymmetry becomes critical in real measurements.

| Gas | $\int (\text{Theo} - \text{Meas})_{\text{fill}}$ | $\int (\text{Theo} - \text{Meas})_{\text{empty}}$ | difference | $\lambda_{\text{fill}}$ | $\lambda_{\text{empty}}$ |
|---|---|---|---|---|---|
| $NH_3$ | 16.23 | -16.33 | -0.20 | 5.40 | 0.36 |
| $NO_2$ | 13.40 | -13.64 | -0.23 | 3.04 | 0.40 |
| HONO | 13.57 | -13.65 | -0.05 | 3.14 | 0.40 |

## S8. References


Burkholder, J. B., Sander, S. P., Abbatt, J. P. D., Barker, J. R., Cappa, C., Crounse, J. D., Dibble, T. S., Huie, R. E., Kolb, C. E., Kurylo, M. J., Orkin, V. L., Percival, C. J., Wilmout, D. M., and Wine, P. H.: Chemical Kinetics and Photochemical Data for Use in Atmospheric Studies – Evaluation Number 19, NASA JPL Publication 19-5, Tables 4C-1-2, 4C-1-3, and 4C-7-2, https://jpldataeval.jpl.nasa.gov/, (last accessed: 2026-03-25), 2020.

Crilley, L. R., Lao, M., Salehpoor, L., and VandenBoer, T. C.: Emerging investigator series: an instrument to measure and speciate the total reactive nitrogen budget indoors: description and field measurements, Environ. Sci.: Processes Impacts, 25, 389–404, https://doi.org/10.1039/d2em00446a, 2023.

Ebnesajjad, S.: Introduction to fluoropolymers, in: Applied Plastics Engineering Handbook: Processing, Materials, and Applications, 2nd edn., edited by: Kutz, M., Elsevier, 55–71, https://doi.org/10.1016/B978-0-323-39040-8.00003-1, 2017.

Ellis, R. A., Murphy, J. G., Pattey, E., van Haarlem, R., O'Brien, J. M., and Herndon, S. C.: Characterizing a Quantum Cascade Tunable Infrared Laser Differential Absorption Spectrometer (QC-TILDAS) for measurements of atmospheric ammonia, Atmos. Meas. Tech., 3, 397–406, https://doi.org/10.5194/amt-3-397-2010, 2010

George, C., Ammann, M., D'Anna, B., Donaldson, D. J., and Nizkorodov, S. A.: Heterogeneous photochemistry in the atmosphere, Chem. Rev., 115, 4218–4258, https://doi.org/10.1021/cr500648z, 2015.

Lao, M., Crilley, L. R., Salehpoor, L., Furlani, T. C., Bourgeois, I., Neuman, J. A., Rollins, A. W., Veres, P. R., Washenfelder, R. A., Womack, C. C., Young, C. J., and VandenBoer, T. C.: A portable, robust, stable, and tunable calibration source for gas-phase nitrous acid (HONO), Atmos. Meas. Tech., 13, 5873–5890, https://doi.org/10.5194/amt-13-5873-2020, 2020.

Ma, L., Pascalidou, E. M., Wiame, F., Zanna, S., Maurice, V., and Marcus, P.: Passivation mechanisms and pre-oxidation effects on model surfaces of FeCrNi austenitic stainless steel, Corros. Sci., 167, 108483, https://doi.org/10.1016/J.CORSCI.2020.108483, 2020.

Pape, L., Ammann, C., Nyfeler-Brunner, A., Spirig, C., Hens, K., and Meixner, F. X.: An automated dynamic chamber system for surface exchange measurement of non-reactive and reactive trace gases of grassland ecosystems, Biogeosciences, 6, 405–429, https://doi.org/10.5194/bg-6-405-2009, 2009.

Plake, D., Stella, P., Moravek, A., Mayer, J. C., Ammann, C., Held, A., and Trebs, I.: Comparison of ozone deposition measured with the dynamic chamber and the eddy covariance method, Agr. Forest Meteorol., 206, 97–112, https://doi.org/10.1016/j.agrformet.2015.02.014, 2015.

Salehpoor, L. and VandenBoer, T. C.: Suppressor and calibration standard limitations in cation chromatography of ammonium and 10 alkylamines in atmospheric samples, Anal. Methods, 15, 3822–3842, https://doi.org/10.1039/d3ay01158e, 2023.

Sapag, K., Vallone, A., Blanco, A. A. G., and Solar, C.: Adsorption of methane in porous materials as the basis for the storage of natural gas, in: Natural Gas, edited by: Kumar, S., IntechOpen, https://doi.org/10.5772/9846, 2010.